Fabrication of polycrystalline Weyl antiferromagnetic Mn_3Sn thin films on various seed layers

Takafumi Nakano [1,4], Tomoya Higo [2,4], Ayuko Kobayashi [2,4], Shinji Miwa [2,4,5], Satoru Nakatsuji [2,3,4,5] and Kay Yakushiji [1,4,*]

[1]*National Institute of Advanced Industrial Science and Technology (AIST), Research Center for Emerging Computing Technologies, Tsukuba 305-8568, Japan*
[2]*The Institute for Solid State Physics, The University of Tokyo, Kashiwa 277-8581, Japan*
[3]*Department of Physics, The University of Tokyo, Tokyo 113-0033, Japan*
[4]*CREST, Japan Science and Technology Agency (JST), Saitama 332-0012, Japan*
[5]*Trans-scale Quantum Science Institute, The University of Tokyo, Tokyo 113-0033, Japan*

(Received 5 January 2021; accepted 1 April 2021; published 7 May 2021)

To develop a high-quality Weyl magnet Mn_3Sn thin film, polycrystalline Mn-Sn was sputter deposited onto an fcc or hexagonal close-packed metallic seed layer of Pt, Cu, Ir, Ru, Cr, or Al. Among the tested seed materials, Pt and Cu enabled fabrication of highly *c*-plane oriented textured $D0_{19}$-type Mn_3Sn films with a smooth surface (mean roughness below 0.3 nm) after postannealing at 350 °C or below. The Mn_3Sn films exhibited substantial signals of the anomalous Nernst effect (ANE), which is one characteristic of a Weyl magnet. Microstructural analysis revealed that the Cu seed layer significantly diffused into the Mn_3Sn layer during postannealing, while the Pt seed layer changed little. The results suggested that a small amount of Cu mixture (up to 2.5 at. %) did not degrade the ANE signal but effectively lowered the postannealing temperature to form the $D0_{19}$ structure. The developed films and techniques are beneficial for antiferromagnetic spintronics in terms of the smoothness and process consistency in a standard process for magnetic random-access memory.

DOI: 10.1103/PhysRevMaterials.5.054402

I. INTRODUCTION

Weyl magnet thin films have attracted attention because of their distinctive intrinsic properties, such as the anomalous Hall effect (AHE) [1–6], anomalous Nernst effect (ANE) [7–10], magneto-optical Kerr effect [11], magnetic spin Hall effect (MSHE) [12], and an electrical switching [13], that could enable an advanced spintronics device. Hence, suitable thin-film fabrication technology has been intensively developed for the past few years, especially for the antiferromagnetic Mn_3X (X = Sn, Ge, Ir, Pt, etc.) family. Studies of film formation have been reported for both single- and polycrystalline films, resulting in steps forward such as discovering Weyl-originated features, controlling the crystalline orientation regarding the *c* plane or *m* plane, optimizing the postannealing temperature, and so on [10,14–24].

From the application viewpoint, further demands remain, including a strong crystal orientation, a smooth surface or interface, and controlled interdiffusion at an interface. At the same time, a film on a thermally oxidized silicon substrate must exhibit these features. In particular, improvement of surface smoothness, which is the basis of device performance and reliability, has not been fully investigated: only a couple of values have been reported [10,14,15]. Specifically, to achieve memory function in a three-terminal type magnetic random-access memory (MRAM) by using the MSHE, a Mn_3X spin-Hall bar typically requires a mean surface roughness (R_a) below 0.2 nm. Such smoothness is necessary to obtain a high magnetoresistance ratio and restricted dispersion of the performance for the magnetic tunnel junction (MTJ) cells fabricated above.

We have concluded that an adequate thin film could definitely be fabricated by using information from a previously developed film with a similar structure, orientation, and lattice constant. For example, knowledge of $L1_2$-Mn_3Ir is useful for developing a *c*-plane oriented Mn_3X thin film. Although the space group $Fm^{-}3m$ of $L1_2$-Mn_3Ir is not identical to the $D0_{19}$ crystal structure, whose space group is $P6_3/mmc$, their structures are similar and they can be grown similarly under optimum conditions. In fact, (111)-oriented polycrystalline $L1_2$-Mn_3Ir films have already been used in commercial products: the read head of a hard-disk drive, an MRAM, and a magnetic sensor. An important key for success is selection of a seed layer to effectively induce a specific orientation in the subsequently deposited film: a hexagonal close-packed (hcp) (0001)- or fcc (111)-oriented seed layer of polycrystalline Ru, Pt, Ni-Fe, Cu, or other metals has typically been used, resulting in a strong (111) orientation [25–27]. Furthermore, it has been found that the roughness of the Mn_3Ir film is sensitive to the process gas species during sputtering [28], as well as the lattice matching with the seed layer.

In this study, we systematically investigated the properties of polycrystalline Mn-Sn thin films fabricated with various seed-layer materials. The goal was to obtain a $D0_{19}$-type Mn_3Sn structure with a smooth surface, strong crystal orientation, and low annealing temperature, along with the performance characteristics of a Weyl magnet. For the seed layer, we used fcc or hcp materials having a small lattice mismatch with Mn_3Sn ($a/2 = 2.83$ Å), namely, Pt ($a/\sqrt{2} = 2.76$ Å), Cu ($a/\sqrt{2} = 2.55$ Å), Ir ($a/\sqrt{2} = 2.78$ Å), Ru ($a = 2.70$ Å), Cr ($a = 2.88$ Å), and Al ($a/\sqrt{2} = 2.86$ Å), where a

*k-yakushiji@aist.go.jp

denotes the lattice constant. We predicted that the fabricated Mn-Sn films would exhibit a *c*-plane oriented polycrystalline structure, i.e., a textured structure, after postannealing. Accordingly, we investigated the properties and microstructure of the fabricated samples to determine a suitable seed layer and the conditions required for a device fabrication process.

II. EXPERIMENTAL METHOD

Film deposition was performed at room temperature on a thermally oxidized silicon (001) substrate by using a mass-production sputtering apparatus, the Canon Anelva C-7100, for φ200-mm wafers. The Mn-Sn composition was precisely controlled by adjusting the input-power ratio from two targets: $Mn_{68}Sn_{32}$ and $Mn_{76}Sn_{24}$. The resultant compositions (Mn_xSn_{100-x}) in this study were determined by x-ray fluorescence measurements. Sputter deposition of Mn-Sn film was then performed using Ar, Kr, or Xe process gas. After deposition, the films were postannealed at various temperatures (T_a) for 1 h in a vacuum.

The resulting samples were characterized in several ways. Crystallographic analysis was performed by x-ray diffraction (XRD) using Cu-Kα radiation. The surface roughness was characterized by atomic force microscopy (AFM). The microstructure was observed by high-resolution transmission electron microscopy (HR-TEM), nanoelectron beam diffraction (NBD), and high-angle annular dark-field scanning transmission electron microscopy (HAADF-STEM). Elemental mapping was performed by energy-dispersive x-ray spectroscopy (EDX). The magnetization is measured with a superconducting quantum interference device magnetometer. The Nernst voltage was measured for a blanket film stack with an out-of-plane temperature gradient and an in-plane magnetic field. For Hall effect measurement, the films were microfabricated into micrometer-scale Hall bars by photolithography and then evaluated by a DC four-probe method. All the measurements were performed at room temperature.

III. RESULTS AND DISCUSSION

A. Surface roughness dependence on sputtering gas

First, we checked the variation of surface roughness for various process-gas species during the Mn-Sn sputtering to find the most favorable one. Figure 1(a) shows a schematic of the stacking structure of the samples: substrate/Ta (2 nm)/Ru (2 nm)/Pt (1 nm) seed layer/Mn-Sn (20 nm)/Ta (2 nm). Figure 1(b) shows XRD profiles for postannealed samples (T_a = 350 °C) that suggest formation of hcp *c*-plane oriented Mn_3Sn regardless of the gas species. Note that detailed results for Mn-Sn films with other seed layers are given later in this section. Figures 1(c) and 1(d) show AFM images of sample surfaces obtained by using Ar and Xe gas, respectively, during the Mn-Sn sputtering (gas pressure ~0.1 Pa). The results reveal that a smoother surface and a higher intensity for the (002) and (004) peaks were obtained when the heavier gas species (Xe) was used during sputtering. In particular, the surface roughness changed drastically: the mean surface roughness, R_a (root-mean-square roughness, R_q), was 0.40 (0.54), 0.20 (0.26), and 0.16 (0.21) nm for films deposited with Ar, Kr (not shown in the figure), and Xe, respectively.

We can possibly attribute these differences to the different kinetic energies of the recoiled ions that cause bombardment of the sputtered clusters [28,29]. This factor should affect the film quality: for example, in a previous study on Mn_3Ir, a Kr gas process provided a better crystal structure than an Ar gas process did. In our case, although we have not clarified the details of the gas-species dependence, we found that the best Mn_3Sn film quality, i.e., the best peak intensity and surface smoothness, was obtained with Xe gas. Consequently, we used Xe throughout the rest of this study. Note that the compositions of the Mn-Sn layers were slightly different: $Mn_{77}Sn_{23}$, $Mn_{79}Sn_{21}$, and $Mn_{79}Sn_{21}$ for Ar, Kr, and Xe gas, respectively. Although the roughness tended to decrease when the Mn composition was increased, the difference in R_a due to the gas species (by a factor of about 2 between Ar and Xe) was more significant.

B. Effects of different seed layers

Next, we fabricated film stacks (substrate/seed layer/Mn-Sn layer/capping layer) with various seed-layer structures: Ta (2)/Ru (2) or Ta (2)/Ru (2)/NM (1), where NM denotes either Pt, Cu, Ir, Cr, or Al. The total seed-layer thickness (including the Ta layer) was minimized to reduce the in-plane electric shunts for the Nernst voltage and AHE measurements. Figures 2(a) and 2(b), 2(c) and 2(d), and 2(e) and 2(f) show XRD profiles for samples as deposited and postannealed at T_a = 300 and 350 °C, respectively. In the graphs, the vertical straight lines represent calculated 2θ angles for $D0_{19}$-type Mn_3Sn (002) and (004) at 39.76° and 85.71°, respectively. Overall, a higher annealing temperature yielded higher (002) and (004) peak intensities with Pt, Cu, Ir, Ru, and Cr, but not with Al. The samples annealed at T_a = 350 °C, shown in Figs. 2(e) and 2(f), had no additional peaks originating from other crystal orientations of $D0_{19}$-type Mn_3Sn or impurity phases such as ferromagnetic Mn_2Sn. Some of the peaks slightly shifted from the calculated angles, probably because of lattice distortion induced by the adjacent seed layers. Among the tested seed materials, Pt and Cu obviously induced *c*-plane orientation of the $D0_{19}$-type structure after postannealing at T_a = 350 °C. Furthermore, Cu was the only seed material to induce this structure with a lower T_a (300 °C). This suggests that the Cu seed promoted crystallization of $D0_{19}$-type Mn_3Sn even with a lower T_a, compared with the other materials including Pt that provided the best structures with T_a = 350 °C. The as-deposited films, as shown in Figs. 2(a) and 2(b), only had backgrounds originating from the seed layers and the substrate, implying that the as-deposited Mn-Sn thin films had an amorphous or nanocrystalline structure. In summary, we succeeded in fabricating single-phase $D0_{19}$-type Mn_3Sn with a *c*-plane oriented polycrystal, and we confirmed the importance of choosing a favorable seed-layer material.

In terms of the surface roughness, the seed-layer material (except for Al) and the postannealing temperature hardly affected it, resulting in similar R_a(R_q) values ranging from 0.23–0.26 (0.33–0.36) nm. We confirmed that such a smooth surface was maintained even when the Mn-Sn thickness increased: for example, we obtained an R_a(R_q) value of 0.19

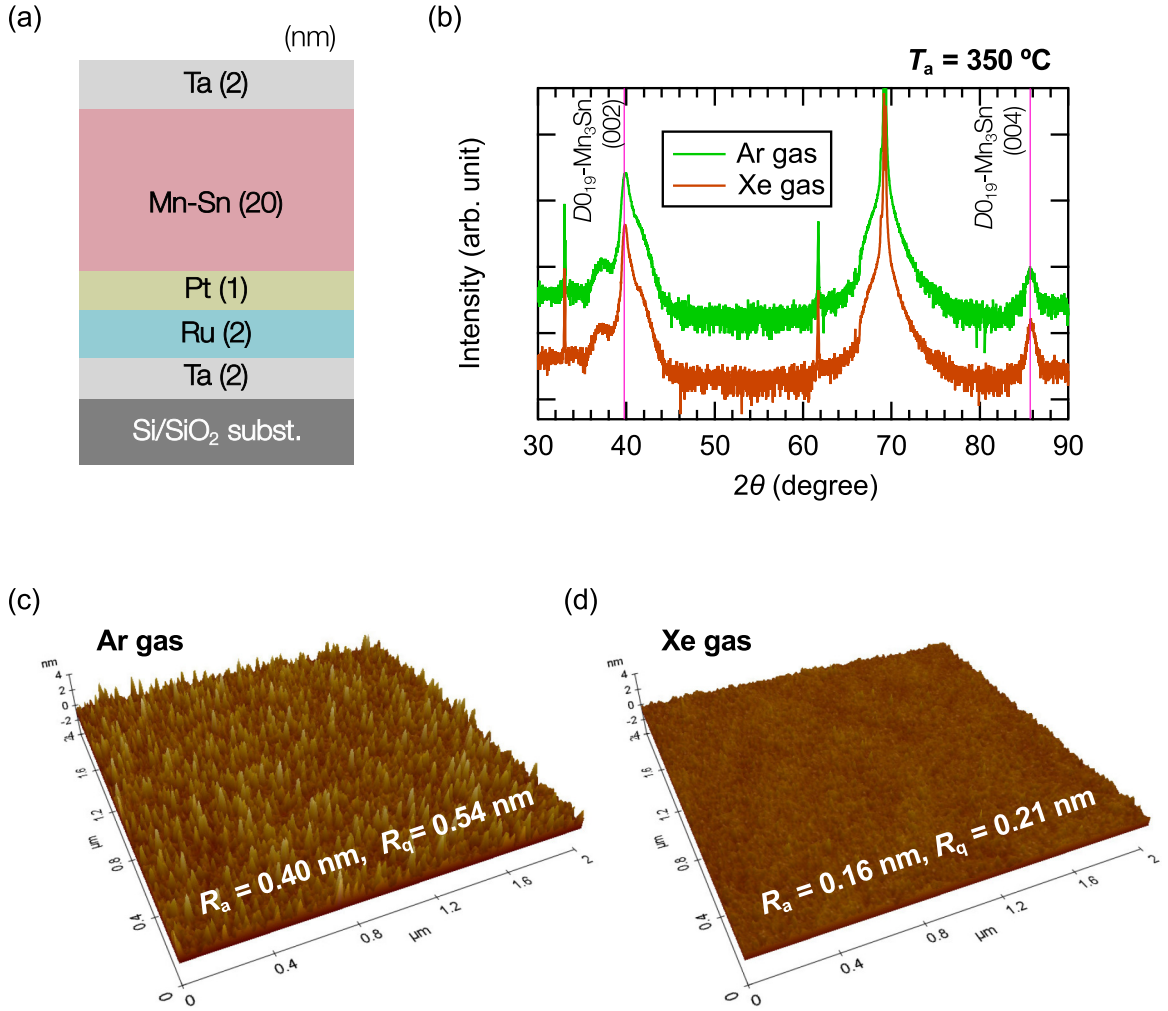

FIG. 1. (a) Schematic illustration of the sample structure. (b) XRD profiles for samples postannealed at 350 °C. The green and brown profiles are for samples obtained by using Ar and Xe gas, respectively, during sputtering. (c), (d) AFM images of sample surfaces obtained with Ar and Xe gas, respectively.

(0.24) nm for a 300-nm-thick Mn-Sn thin film with a Pt seed layer after postannealing at $T_a = 350\,^{\circ}\mathrm{C}$. The R_a values of our films were comparable to the smallest value ever reported ($R_a < 0.2$ nm) for a randomly oriented Mn_3Sn thin film [15]. Such excellent smoothness would be beneficial in building a multilayer structure such as an MTJ on Mn_3Sn thin film. Note that the R_a and R_q for the sample with the Pt seed layer were not identical but slightly rougher compared to the values shown in Fig. 1. We attribute this roughness change to the difference in the Mn-Sn layer's composition: $Mn_{75}Sn_{25}$ in this case but $Mn_{79}Sn_{21}$ for the Fig. 1 sample. As described above, the decreased Mn content in this case led to the slight increase in R_a and R_q.

C. Microstructural analysis

For the samples with Pt and Cu seed layers, microstructural analysis was performed. Figures 3(a) and 3(b) show cross-sectional TEM images of the samples ($T_a = 350\,^{\circ}\mathrm{C}$) with Pt and Cu, respectively. The Mn-Sn layers in these samples were continuous and smooth at both the upper and lower interfaces. Moreover, the TEM images revealed that the Mn-Sn layers grew with a highly hcp c-plane oriented texture on the seed layer. NBD analysis, as shown in the insets of Figs. 3(a) and 3(b), confirmed the crystal structures as c-plane oriented $D0_{19}$-type Mn_3Sn, which is consistent with the XRD results shown in Figs. 2(e) and 2(f). Corresponding to the HR-TEM images in Figs. 3(a) and 3(b), respectively, Figs. 3(c) and 3(d) show high-resolution HAADF-STEM images (leftmost) of the Mn-Sn layers, together with EDX mappings for Ta, Ru, Pt, Mn, and Sn. The HAADF-STEM image in Fig. 3(e) reveals uniform atomic ordering of Mn and Sn in accordance with the $D0_{19}$-type structure. Note the apparent oxidation in the upper parts of both Mn-Sn layers just beneath the Ta capping layers as identified by the bright contrast in the HAADF-STEM images [Figs. 3(c) and 3(d)]. This result suggests that the thickness of the Ta capping layer (∼2 nm) was insufficient to block oxygen penetration from the top surface, yet the oxidation stopped at the small upper region of the Mn-Sn layer.

Interestingly, the EDX mappings revealed that the Pt and Cu seed layers showed quite distinct behaviors. The Cu seed

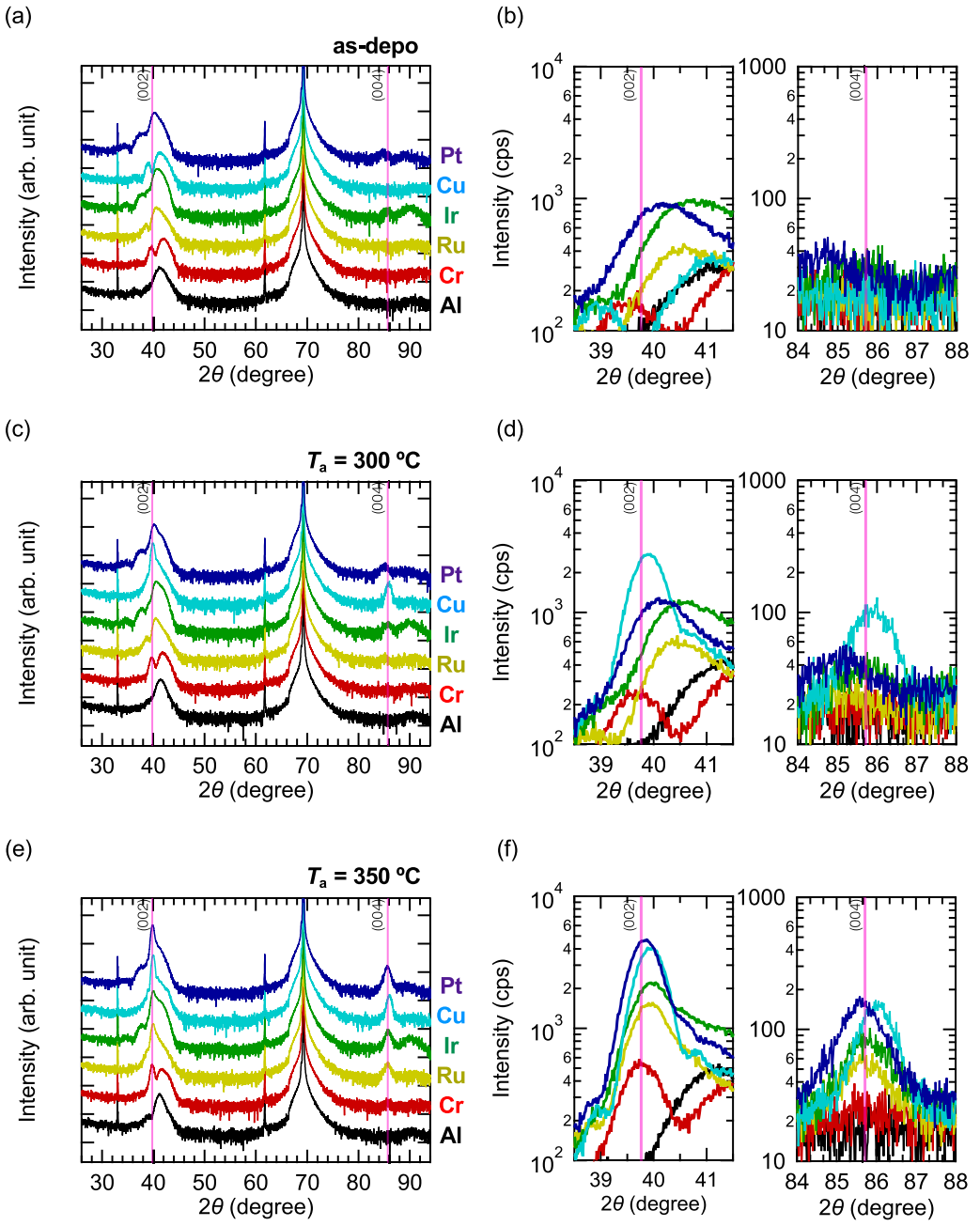

FIG. 2. XRD profiles of samples obtained with various seed layers: (a), (b) as deposited; (c), (d) after postannealing at $T_a = 300\,^{\circ}$C; and (e), (f) after postannealing at $T_a = 350\,^{\circ}$C. (b), (d), and (f) show magnified profiles around the Mn_3Sn (002) and (004) angles.

layer totally deteriorated and intermixed with the adjoining Mn-Sn layer, while the Pt seed layer maintained sharp interfaces that probably provided a good template for Mn-Sn growth. Thus, we should carefully investigate the template effect for the Cu seed case. Here we consider two possibilities for promoting $D0_{19}$-type Mn_3Sn. One is that the template effect of Cu begins at a low temperature, and the crystalline Mn_3Sn part, even for a few atomic layers, continues growing with the remaining Mn-Sn part as the template after degrading the Cu layer. Another possibility is that the Cu seed layer immediately disappears at an early stage of postannealing (including the as-deposited state) and then the Ru underlayer provides the template. Note the high natural solubility between Cu and Mn, which are soluble at all proportions [30]. Although we have not clarified when the Cu layer lost the template effect in the fabrication process, the XRD results in Fig. 2(c) demonstrated that the sample with the Cu seed only formed $D0_{19}$-type Mn_3Sn at a low T_a (300 °C). Those results suggest that the Cu mixing in the Mn-Sn layer effectively acted to lower the temperature required for the crystalline or chemical ordering of the $D0_{19}$-type structure.

D. Effect of Cu mixing

To investigate the details of the Cu mixing effect, we fabricated new samples by varying the thickness of the Cu seed

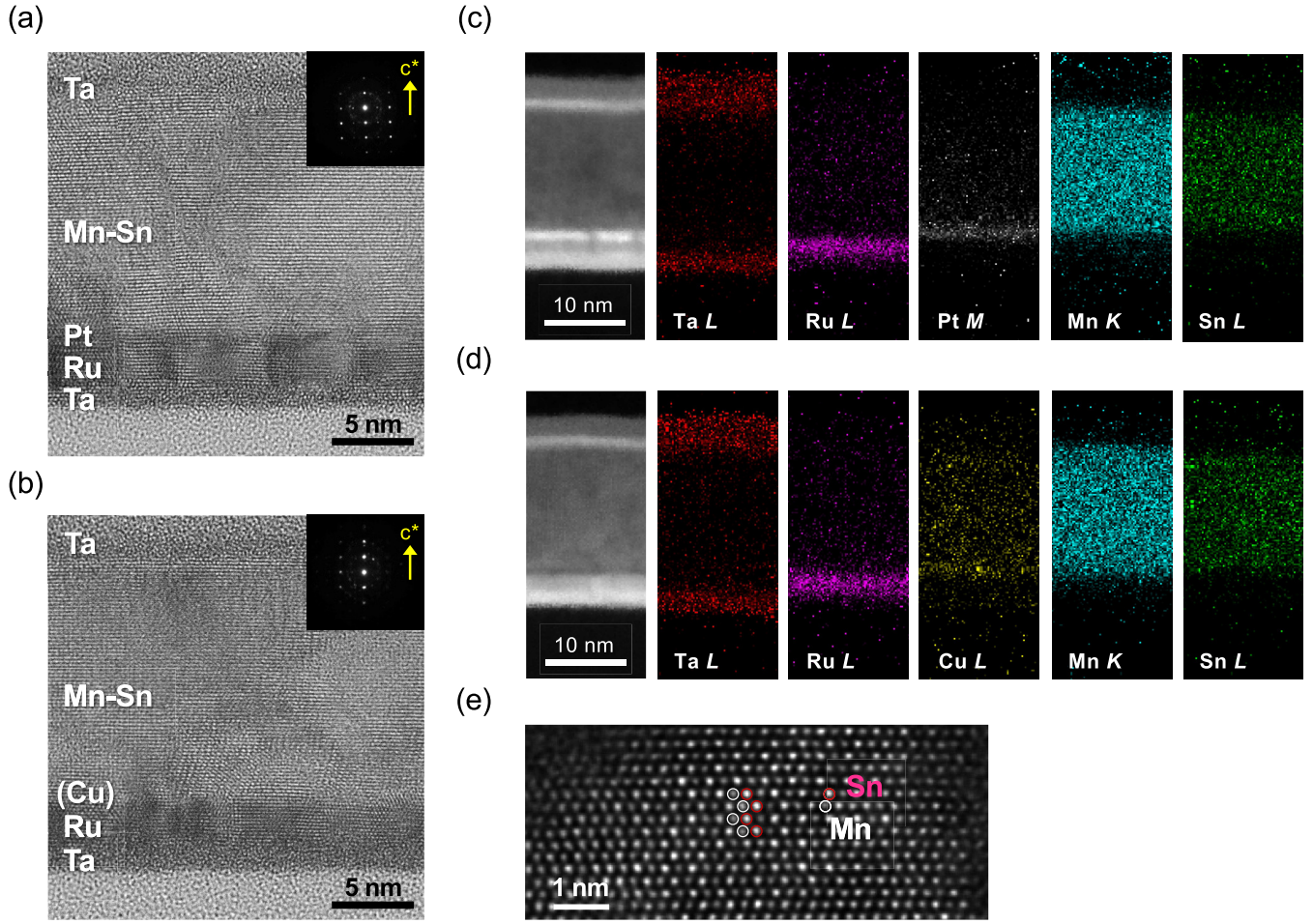

FIG. 3. Cross-sectional TEM images of samples ($T_a = 350\,^{\circ}$C) with (a) Pt and (b) Cu seed layers. The insets show NBD patterns of the Mn-Sn layers. (c), (d) HAADF-STEM images (leftmost) and EDX profiles for the corresponding samples shown in (a) and (b), respectively. (e) High-resolution HAADF-STEM image of part of the Mn-Sn layer shown in (a).

layer. The stacking structure was as follows: substrate/$Ta_{80}B_{20}$ (3)/Ru (2)/Pt (1)/Cu (0, 2, 5)/Mn-Sn (195, 198, 200)/Pt capping layer (3). In this structure, the seed layer was a Pt/Cu bilayer to benefit from both constituents' roles: Pt as a template and Cu as a doping material for Mn-Sn. The thickness of the Mn-Sn layer was adjusted to fix the total thickness of Cu/Mn-Sn at 200 nm, resulting in Cu content of 0, 1.0, or 2.5 at. % in the mixed Mn-Sn-Cu layer. Note that the Mn-Sn thickness was 10 times thicker than in the previous samples to give a small amount of Cu mixture.

Figures 4(a) and 4(b) show XRD profiles of control samples annealed at $T_a = 300\,^{\circ}$C. The Cu mixture samples exhibited clear $D0_{19}$-type Mn_3Sn (002) and (004) peaks, and higher Cu content gave peaks with higher intensities. We found that the Cu mixture was remarkably effective to induce crystallization of $D0_{19}$-type Mn_3Sn. Note that the as-deposited films exhibited no Mn_3Sn peaks (not shown here). On the other hand, in the samples annealed at $T_a = 350\,^{\circ}$C, the Cu mixing effect caused a different trend shown in Figs. 4(c) and 4(d). The magnified profiles around the (002) peak in Fig. 4(d) reveal a decrease in the (002) peak intensity as the Cu concentration is increased. This result suggests a senario in which the growth of $D0_{19}$-type Mn_3Sn was completed by using the template of the Pt seed layer, after which a Cu atom acted as an impurity and caused a lattice distortion, exhibited as a peak angle shift. Nevertheless, this was a minor effect because even the sample with the highest Cu content exhibited a substantial intensity. Note also the importance of ensuring that Cu impurities do not degrade the crystallinity of Mn_3Sn. Consequently, these results could provide a new approach to form a Mn_3Sn thin film at a low annealing temperature by doping a third element, although it may still require clarifying the mechanisms of the Cu mixing effect, such as promoting crystallization of $D0_{19}$-type Mn_3Sn and lowering the annealing temperature.

E. Magnetotransport properties

Finally, we evaluated the magnetotransport properties at 300 K for the samples with Pt seed/Mn-Sn (400) and Cu seed/Mn-Sn (400) at $T_a = 350\,^{\circ}$C to investigate whether the samples (including the Cu mixture ones) exhibit the features of a Weyl magnet. From the viewpoint of crystal orientation, the c plane of $D0_{19}$-Mn_3X (X = Sn, Ge), consisting of a Kagome lattice of Mn atoms, should provide the sizable ANE for the in-plane (i.e., along the ab plane of $D0_{19}$−Mn_3Sn)

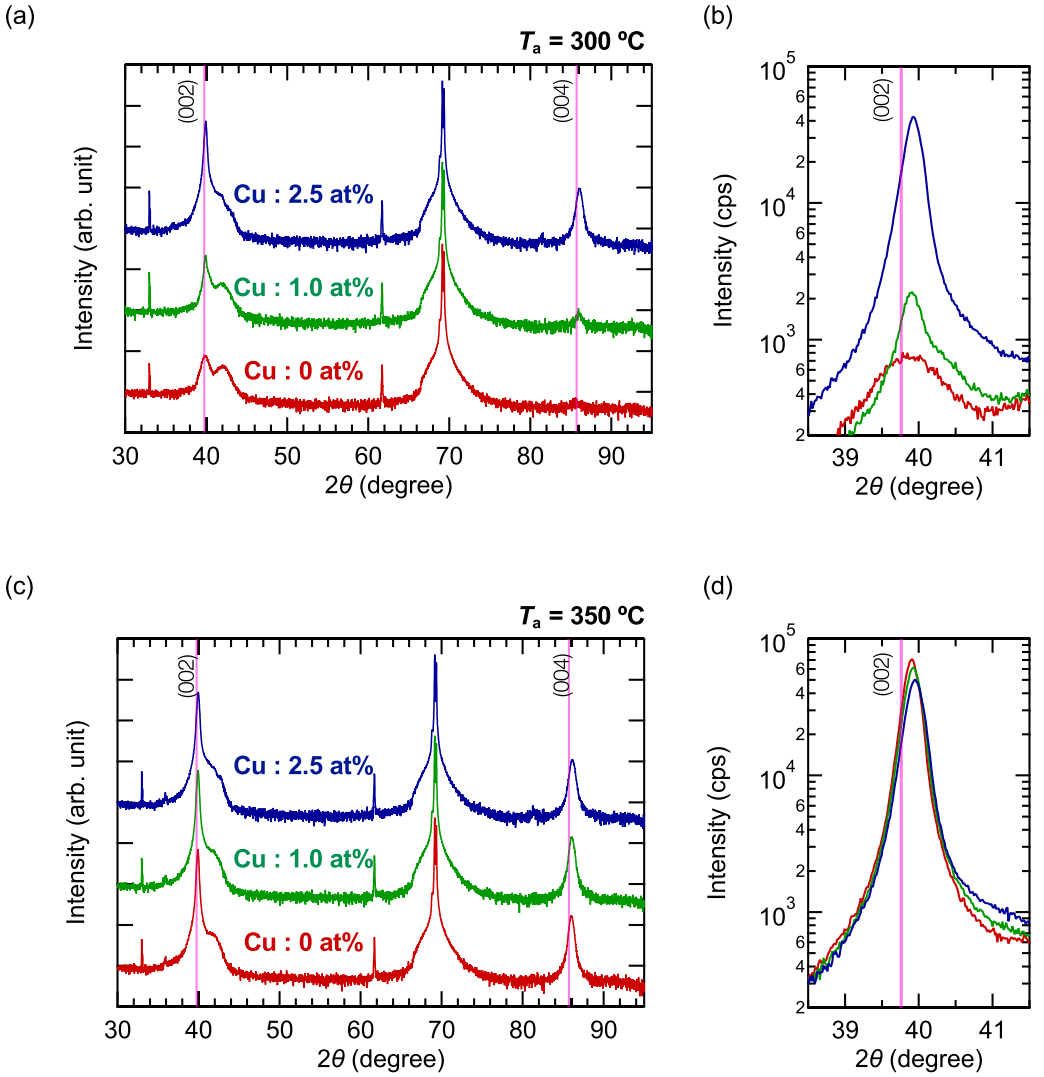

FIG. 4. XRD profiles of samples with a Cu seed layer for (a), (b) $T_a = 300\,^{\circ}$C and (c), (d) $T_a = 350\,^{\circ}$C. The notations 0, 1.0, and 2.5 at. % indicate the Cu content in the Cu/Mn-Sn bilayer, because the Cu layer totally intermixed with the adjoining Mn-Sn layer after postannealing. (b), (d) Magnified profiles around the angle of Mn_3Sn (002).

magnetic field. Before performing the magnetotransport measurement, we checked antiferromagnetic behavior at room temperature for the fabricated films. The magnetization curves with in-plane magnetic field shown in Fig. 5(a) revealed vanishingly small magnetization and the hysteric behavior with the spontaneous component of several mμ_B per formula unit, that are consistent with the reported weak ferromagnetism for $D0_{19}$-Mn_3Sn bulk [5–7] and film [17,30] samples. Then the ANE voltage (V_{ANE}) was evaluated. The results and the schematic of the setup are shown in Fig. 5(b). In the measurement, the film's in-plane voltage, V_{ANE}, was measured by sweeping the in-plane magnetic field applied perpendicular to the terminals for V_{ANE} (the distance, $d = 5.5$ mm) at a fixed thermal gradient in the sample including the substrate ($\nabla T \sim 2$ K/mm) applied in the out-of-plane direction [31]. The results showed the saturated V_{ANE} values of 1.95 and 1.75 μV, indicating the anomalous Nernst coefficients (S_{ANE}) to be 0.22 and 0.20 μV/K for the Mn-Sn with Pt and Cu seeds, respectively (estimation of the coefficient is given later). These values are consistent with the reported values for Mn_3Sn bulk [7–9] and film [13,14] samples, suggesting comparable crystallographic quality to the Weyl magnet. Interestingly, the sample with the Cu seed exhibited a substantial S_{ANE} despite the Cu intermixing in the whole Mn-Sn layer. This result suggests that the Cu mixing did not disturb the performance of the topological feature of a Weyl material. Note that a value of the gradient in the films ∇T_{film} is necessary to estimate an $S_{ANE}(= V_{ANE}/d/\nabla T_{film})$; however, ∇T_{film} is not easy to decide because thermal gradient majorly occurs in the substrate. To decide ∇T_{film}, we utilized a reference sample with the 400-nm-thick randomly oriented polycrystalline film on a Si/SiO_2 substrate [32],whose S_{ANE} was determined in advance as $\sim$0.25 μV/K under in-plane thermal gradient. The reference sample showed $V_{ANE} = 2.3\,\mu$V, which provided $\nabla T_{film} \sim 1.6$ K/mm in the same experimental condition with out-of-plane thermal gradient ($\nabla T \sim 2$ K/mm, and $d = 5.5$ mm). Lastly, the AHE was evaluated. Figure 5(c) shows the magnetic-field dependence of the Hall resistivity (ρ_{yx}). When

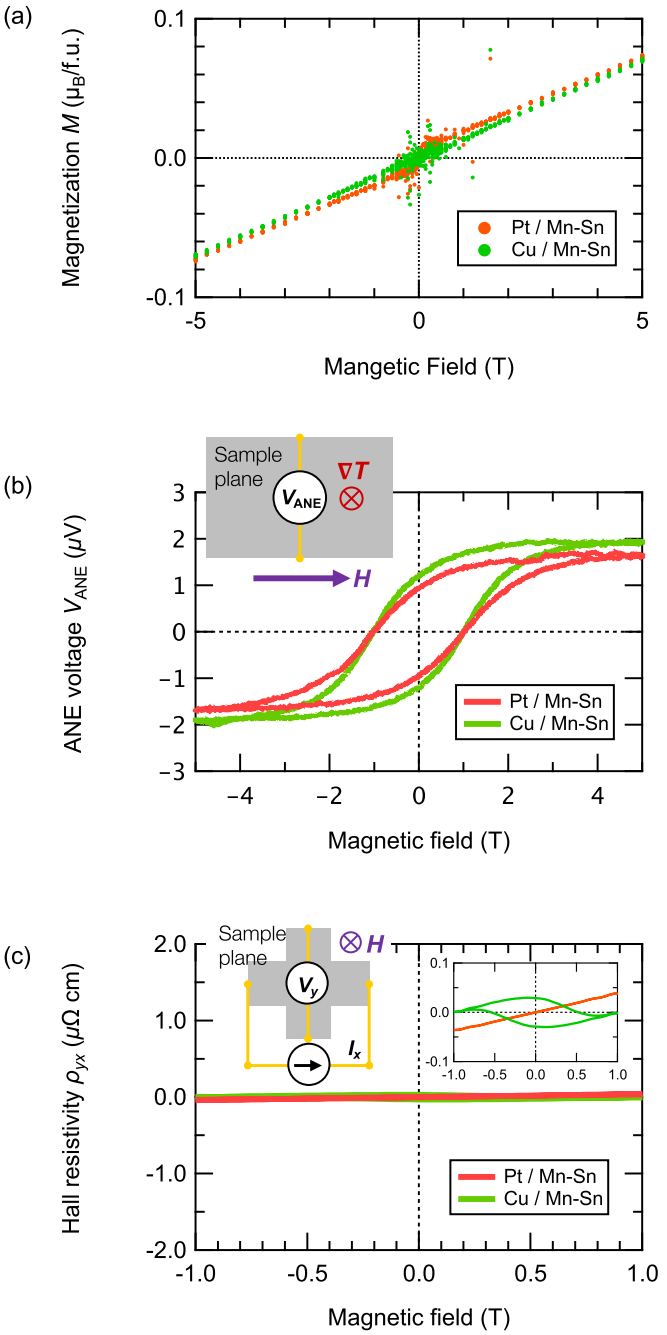

FIG. 5. Properties for samples with Pt and Cu seed layers measured at 300 K. (a) Mangetization curves after annealing at 350 °C. The magnetic field is applied along the film plane. (b) Magnetic-field dependence of the ANE voltage (V_{ANE}) at a temperature gradient ∇T of 2 K/mm. The inset illustrates the parametric directions in the measurement setup. (c) Magnetic-field dependence of the Hall resistivity (ρ_{yx}). The right and left inset show magnified curves and the measurement setup, respectively.

a $D0_{19}$-Mn_3Sn film is perfectly c-plane oriented, the AHE signal is expected to respond to the magnetic field applied within the c plane (i.e., the film's in-plane direction). In such a case, the signal can be detected only in the vertical direction, and there is no signal in the horizontal direction when an out-of-plane field is applied [1]. In this study, we used the measurement setup in the latter case, as shown schematically in the left inset; thus, the electric transport in the horizontal direction was measured by applying an out-of-plane field. The Hall resistivity, ρ_{yx}, is defined as $V_y t/I_x$, where V_y, t, and I_x denote the transverse voltage, thickness, and current, respectively. In the graph, the maximum value on the vertical axis is set to 2 $\mu\Omega$ cm, which corresponds to typical AHE values reported for randomly oriented polycrystalline Mn_3Sn thin films [14,23,24]. Compared with the reported values, the AHE signals of our films were two orders smaller: $\rho_{yx} \sim 0.0$ and 0.04 $\mu\Omega$ cm for the Pt- and Cu-seed samples, respectively. Such negligibly small signals demonstrate that the fabricated films mostly consisted of highly c-plane oriented grains as suggested by the XRD analysis. Deeper examination of the AHE results reveals a hysteresis for the Cu-seed sample with nonzero ρ_{yx} (0.04 $\mu\Omega$ cm) as shown in the magnified graph (the right inset). The hysteresis indicates the existence of a small orientation slant or the emergence of a different phase, because of the Cu mixing.

To sum up the ANE, AHE, and magnetization evaluation, samples with Pt and Cu seed layers both displayed reasonable performance as a Weyl-material, as well as strong c-plane orientation and a smooth surface, making them suitable for spintronic applications.

IV. SUMMARY

Highly c-plane oriented polycrystalline Mn-Sn films were sputter deposited on an fcc or hcp metallic seed layer consisting of Pt, Cu, Ir, Ru, Cr, or Al. Among these seed materials, Pt and Cu provided large XRD (002) and (004) peak intensities from $D0_{19}$-type Mn_3Sn after postannealing at 350 °C or below. In addition, the film surfaces were very smooth (mean roughness below 0.3 nm) when Xe gas was used for the sputtering process. These high-quality films exhibited substantial signals of the anomalous Nernst effect (ANE), which is a notable characteristic of a Weyl magnet. Microstructural analysis revealed that the Cu seed layer significantly diffused into the Mn_3Sn layer during the postannealing, while the Pt seed layer changed little. The results suggested that a small amount of the Cu mixture (up to 2.5 at. %) did not degrade the ANE signal but effectively lowered the postannealing temperature to form the $D0_{19}$ structure. The developed films and techniques are beneficial for antiferromagnetic spintronics in terms of the smoothness and process consistency in a standard MRAM process.

ACKNOWLEDGMENTS

We would like to thank Prof. YoshiChika Otani for fruitful discussions. This work was supported in part by CREST (Grant No. JPMJCR18T3), Japan Science and Technology Agency.

[1] S. Nakatsuji, N. Kiyohara, and T. Higo, Large anomalous Hall effect in a non-collinear antiferromagnet at room temperature, Nature (London) **527**, 212 (2015).

[2] N. Kiyohara, T. Tomita, and S. Nakatsuji, Giant Anomalous Hall Effect in the Chiral Antiferromagnet Mn_3Ge, Phys. Rev. Appl. **5**, 064009 (2016).

[3] A. K. Nayak, J. E. Fischer, Y. Sun, B. H. Yan, J. Karel, A. C. Komarek, C. Shekhar, N. Kumar, W. Schnelle, J. Kubler, C. Felser, and S. S. P. Parkin, Large anomalous Hall effect driven by a nonvanishing Berry curvature in the noncolinear antiferromagnet Mn_3Ge, Sci. Adv. **2**, e1501870 (2016).

[4] Y. Zhang, Y. Sun, H. Yang, J. Zelezny, S. P. P. Parkin, C. Felser, and B. H. Yan, Strong anisotropic anomalous Hall effect and spin Hall effect in the chiral antiferromagnetic compounds Mn_3X ($X =$ Ge, Sn, Ga, Ir, Rh, and Pt), Phys. Rev. B **95**, 075128 (2017).

[5] E. K. Liu, Y. Sun, N. Kumar, L. Muechler, A. L. Sun, L. Jiao, S. Y. Yang, D. F. Liu, A. J. Liang, Q. N. Xu, J. Kroder, V. Suss, H. Borrmann, C. Shekhar, Z. S. Wang, C. Y. Xi, W. H. Wang, W. Schnelle, S. Wirth, Y. L. Chen, S. T. B. Goennenwein, and C. Felser, Giant anomalous Hall effect in a ferromagnetic kagome-lattice semimetal, Nat. Phys. **14**, 1125 (2018).

[6] Z. Guguchia, J. A. T. Verezhak, D. J. Gawryluk, S. S. Tsirkin, J. X. Yin, I. Belopolski, H. Zhou, G. Simutis, S. S. Zhang, T. A. Cochran, G. Chang, E. Pomjakushina, L. Keller, Z. Skrzeczkowska, Q. Wang, H. C. Lei, R. Khasanov, A. Amato, S. Jia, T. Neupert, H. Luetkens, and M. Z. Hasan, Tunable anomalous Hall conductivity through volume-wise magnetic competition in a topological kagome magnet, Nat. Commun. **11**, 559 (2020).

[7] M. Ikhlas, T. Tomita, T. Koretsune, M. T. Suzuki, D. Nishio-Hamane, R. Arita, Y. Otani, and S. Nakatsuji, Large anomalous Nernst effect at room temperature in a chiral antiferromagnet, Nat. Phys. **13**, 1085 (2017).

[8] H. Narita, M. Ikhlas, M. Kimata, A. A. Nugroho, S. Nakatsuji, and Y. Otani, Anomalous Nernst effect in a microfabricated thermoelectric element made of chiral antiferromagnet Mn_3Sn, Appl. Phys. Lett. **111**, 202404 (2017).

[9] X. Li, L. Xu, L. Ding, J. Wang, M. Shen, X. Lu, Z. Zhu, and K. Behnia, Anomalous Nernst and Righi-Leduc Effects in Mn_3Sn: Berry Curvature and Entropy Flow, Phys. Rev. Lett. **119**, 056601 (2017).

[10] H. Reichlova, T. Janda, J. Godinho, A. Markou, D. Kriegner, R. Schlitz, J. Zelezny, Z. Soban, M. Bejarano, H. Schultheiss, P. Nemec, T. Jungwirth, C. Felser, J. Wunderlich, and S. T. B. Goennenwein, Imaging and writing magnetic domains in the non-collinear antiferromagnet Mn_3Sn, Nat. Commun. **10**, 5459 (2019).

[11] T. Higo, H. Y. Man, D. B. Gopman, L. Wu, T. Koretsune, O. M. J. van't Erve, Y. P. Kabanov, D. Rees, Y. F. Li, M. T. Suzuki, S. Patankar, M. Ikhlas, C. L. Chien, R. Arita, R. D. Shull, J. Orenstein, and S. Nakatsuji, Large magneto-optical Kerr effect and imaging of magnetic octupole domains in an antiferromagnetic metal, Nat. Photonics **12**, 73 (2018).

[12] M. Kimata, H. Chen, K. Kondou, S. Sugimoto, P. K. Muduli, M. Ikhlas, Y. Omori, T. Tomita, A. H. MacDonald, S. Nakatsuji, and Y. Otani, Magnetic and magnetic inverse spin Hall effects in a non-collinear antiferromagnet, Nature (London) **565**, 627 (2019).

[13] H. Tsai, T. Higo, K. Kondou, T. Nomoto, A. Sakai, A. Kobayashi, T. Nakano, K. Yakushiji, R. Arita, S. Miwa, Y. Otani, and S. Nakatsuji, Electrical manipulation of a topological antiferromagnetic state, Nature (London) **580**, 608 (2020).

[14] T. Higo, D. R. Qu, Y. F. Li, C. L. Chien, Y. Otani, and S. Nakatsuji, Anomalous Hall effect in thin films of the Weyl antiferromagnet Mn_3Sn, Appl. Phys. Lett. **113**, 202402 (2018).

[15] T. Ikeda, M. Tsunoda, M. Oogane, S. Oh, T. Morita, and Y. Ando, Anomalous Hall effect in polycrystalline Mn_3Sn thin films, Appl. Phys. Lett. **113**, 222405 (2018).

[16] Z. Q. Liu, H. Chen, J. M. Wang, J. H. Liu, K. Wang, Z. X. Feng, H. Yan, X. R. Wang, C. B. Jiang, J. M. D. Coey, and A. H. MacDonald, Electrical switching of the topological anomalous Hall effect in a non-collinear antiferromagnet above room temperature, Nat. Electron. **1**, 172 (2018).

[17] A. Markou, J. M. Taylor, A. Kalache, P. Werner, S. S. P. Parkin, and C. Felser, Noncollinear antiferromagnetic Mn_3Sn films, Phys. Rev. Mater. **2**, 051001(R) (2018).

[18] S. Oh, T. Morita, T. Ikeda, M. Tsunoda, M. Oogane, and Y. Ando, Controlled growth and magnetic property of a-plane-oriented Mn_3Sn thin films, AIP Adv. **9**, 035109 (2019).

[19] Y. You, X. Chen, X. Zhou, Y. Gu, R. Zhang, F. Pan, and C. Song, Anomalous hall effect-like behavior with in-plane magnetic field in noncollinear antiferromagnetic Mn_3Sn films, Adv. Electron. Mater. **5**, 1800818 (2019).

[20] T. Ikeda, M. Tsunoda, M. Oogane, S. Oh, T. Morita, and Y. Ando, Improvement of large anomalous Hall effect in polycrystalline antiferromagnetic $Mn_{3+x}Sn$ thin films, IEEE Trans. Magn. **55**, 2501704 (2019).

[21] A. Kobayashi, T. Higo, S. Nakatsuji, and Y. Otani, Structural and magnetic properties of Mn_3Ge films with Pt and Ru seed layers, AIP Adv. **10**, 015225 (2020).

[22] H. Iwaki, M. Kimata, T. Ikebuchi, Y. Kobayashi, K. Oda, Y. Shiota, T. Ono, and T. Moriyama, Large anomalous Hall effect in L1(2)-ordered antiferromagnetic Mn3Ir thin films, Appl. Phys. Lett. **116**, 022408 (2020).

[23] J. Yoon, Y. Takeuchi, R. Itoh, S. Kanai, S. Fukami, and H. Ohno, Crystal orientation and anomalous Hall effect of sputter-deposited non-collinear antiferromagnetic Mn_3Sn thin films, Appl. Phys. Exp. **13**, 013001 (2020).

[24] T. Ikeda, M. Tsunoda, M. Oogane, S. Oh, T. Morita, and Y. Ando, Fabrication and evaluation of highly c-plane oriented Mn_3Sn thin films, AIP Adv. **10**, 015310 (2020).

[25] K. Imakita, M. Tsunoda, and M. Takahashi, Thickness dependence of exchange anisotropy of polycrystalline Mn3Ir/Co-Fe bilayers, J. Appl. Phys. **97**, 10k106 (2005).

[26] M. Tsunoda, K. Imakita, M. Naka, and M. Takahashi, L**1**(2) phase formation and giant exchange anisotropy in Mn_3Ir/Co-Fe bilayers, J. Magn. Magn. Mater. **304**, 55 (2006).

[27] K. Komagaki, K. Yamada, K. Noma, H. Kanai, K. Kobayashi, Y. Uehara, M. Tsunoda, and M. Takahashi, Large exchange bias and high blocking temperature of MgO-Barrier-MTJs with L1(2)-ordered Mn(3)Ir, IEEE Trans. Magn. **43**, 3535 (2007).

[28] K. Imakita, K. Kobayashi, K. Ono, T. Morita, T. Yamamoto, S. Misawa, and H. Murakami, Effect of Sputtering Gases on the L12 Phase Formation of Mn3Ir/Co-Fe Bilayers, J. Magn. Soc. Jpn. **32**, 291 (2008).

[29] S. Iwatsubo, T. Takahashi, and M. Naoe, Magnetic properties of Fe films deposited by Ar, Kr, and Xe ion beam sputtering, J. Appl. Phys. **83**, 6667 (1998).

[30] N. A. Gokcen, The Cu-Mn (copper-manganese) system, J. Phase Equilib. **14**, 76 (1993).

[31] D. Qu, T. Higo, T. Nishikawa, K. Matsumoto, K. Kondou, D. Nishio-Hamane, R. Ishii, P. K. Muduli, Y. Otani, and S. Nakatsuji, Large enhancement of the spin Hall effect in Mn metal by Sn doping, Phys. Rev. Mater. **2**, 102001(R) (2018).

[32] T. Higo, Y. F. Li, K. Kondou, D. R. Qu, M. Ikhlas, R. Uesugi, D. Nishio-Hamane, C. L. Chien, Y. Otani, and S. Nakatsuji, Omnidirectional control of large electrical output in a topological antiferromagnet, Adv. Funct. Mater. **31**, 2008971 (2021).